Hierarchical transport networks optimizing dynamic response of permeable energy-storage materials

Robert H. Nilson and Stewart K. Griffiths
Physical and Engineering Sciences Center, Sandia National Laboratories, P.O. Box 969, Livermore, California 94550, USA
(Received 16 April 2009; published 17 July 2009)

Channel widths and spacing in latticelike hierarchical transport networks are optimized to achieve maximum extraction of gas or electrical charge from nanoporous energy-storage materials during charge and discharge cycles of specified duration. To address a range of physics, the effective transport diffusivity is taken to vary as a power, m, of channel width. Optimal channel widths and spacing in all levels of the hierarchy are found to increase in a power-law manner with normalized system size, facilitating the derivation of closed-form approximations for the optimal dimensions. Characteristic response times and ratios of channel width to spacing are both shown to vary by the factor $2/m$ between successive levels of any optimal hierarchy. This leads to fractal-like self-similar geometry, but only for $m=2$. For this case of quadratic dependence of diffusivity on channel width, the introduction of transport channels permits increases in system size on the order of 10^4, 10^8, and 10^{10}, without any reduction in extraction efficiency, for hierarchies having 1, 2 and, 8 levels, respectively. However, we also find that for a given system size there is an optimum number of hierarchical levels that maximizes extraction efficiency.

DOI: 10.1103/PhysRevE.80.016310 PACS number(s): 47.56.+r, 47.61.−k, 89.75.Hc, 82.47.Uv

I. INTRODUCTION

Previous studies aimed at optimizing transport in hierarchical networks have addressed steady flow in branching networks like those occurring naturally in vascular systems [1], leaf veins, and river drainage basins [2]. The same physics are operative in branching networks that supply water, gas, and electricity to industrial societies and in engineered materials intended to provide optimal heat extraction [3], fluid distribution [3], or catalysis [4]. These networks are typically constructed in a manner that minimizes the work required to supply a system of given size subject to constraints on the volume of circulating fluid or the cost of materials needed to construct the network. Prior studies of this optimization problem have identified fractal relationships between channel sizes and lengths in different levels of the hierarchy and explained how these features scale with system size [1–6].

In contrast to these earlier studies of steady-state transport, the present paper addresses the transient response of hierarchical channel networks that facilitate rapid charge and discharge of nanoporous materials intended for storage of gas or electric charge. Networks optimized for such transient processes differ from their steady counterparts because the transient case is characterized by a time for transport along channels that varies with the square of channel length, whereas the steady case is characterized by a resistance to flow that varies just linearly with length.

The topology of the latticelike networks addressed here and in one earlier study [7] also differs from that of previously studied treelike structures that connect a centrally located point source to its surroundings. The alternative purpose of the latticelike network architecture in Fig. 1 is to connect the interior of a permeable storage reservoir to one or more of its boundaries. Networks having this type of connectivity can now be engineered into nanoporous materials using fabrication processes that produce multiple scales of porosity by phase segregation, templating, self-assembly, and multiscale aggregation processes [8].

Here we determine the channel sizes, spacing, and order of hierarchy that yield maximum extraction of gas or electric charge from a permeable material of fixed total volume during periodic charge/discharge cycles having prescribed period. High storage densities are best achieved in molecular scale nanopores that provide very large surface areas and functionality unavailable in larger channels. However, these small pores also tend to inhibit long-range transport because effective transport diffusivities generally decrease with decreasing pore size. The introduction of wider transport channels helps to shorten response time, but it also consumes a portion of the volume that would otherwise be available for high-capacity nanopore storage. Thus, optimization is needed to balance the opposing goals of large system capacity and rapid response.

II. GOVERNING EQUATIONS

In the idealized geometry of Fig. 1, the smallest pores have width a_0, center-to-center spacing b_0, bulk porosity

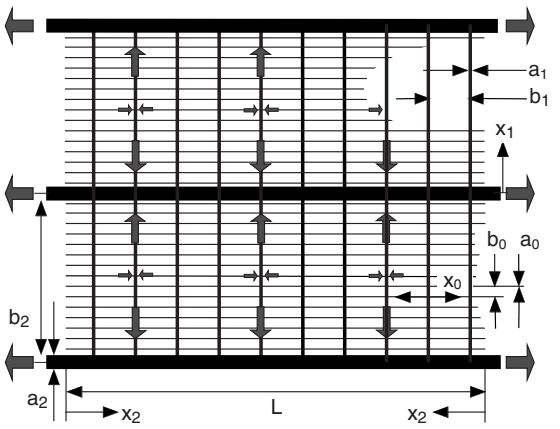

FIG. 1. Latticelike network having nanoscale storage pores and two levels of transport channels, $N=2$.

$\phi_0 = a_0/b_0$, pore length b_1, and diffusion coefficient D_0. These nanopores are connected to an orthogonal network of wider and sparser channels having width and spacing a_1 and b_1, porosity $\phi_1 = a_1/b_1$, diffusivity D_1, and so on. Hierarchies of higher order are constructed by recursive introduction of additional channels, each orthogonal to those of the preceding level. All channels are assumed to be planar slits.

Gas flow or ion transport within each of the smallest pores can generally be described by an equation of the form [9–15]

$$\beta_0 \frac{\partial \rho}{\partial t} = D_0 \frac{\partial^2 \rho}{\partial x_0^2}, \tag{1}$$

where ρ is the density of gas molecules or ions, t is time, x_0 is distance from pore ends, and D_0 is an effective diffusion coefficient. The capacitance β_0 is typically unity for gas transport in large pores, but it may take larger values to account for surface capacitance in electrochemical capacitors or surface adsorption in gas storage materials. In these applications, fluid or ion densities in molecular layers adjacent to pore walls may be several orders greater than those in pore centers [13–17]. As a result, the effective capacitance in Eq. (1) is roughly proportional to the wetted perimeter divided by the cross-sectional area, i.e., $\beta_0 \propto 2/a_0$. Distinct from the diffusion coefficient, D_0, the effective diffusivity is defined as $\alpha_0 = D_0/\beta_0$.

Transport coefficients are fairly well known for a number of important applications. In viscous flow, $D_0 = a_0^2 P_0/12\mu$ where P_0 and μ are the mean pressure and viscosity [9–11]. However, when pore widths are small compared to the mean free path, Λ, the appropriate diffusion coefficient is given by the Knudsen expression, $D_0 \propto \nu a_0$, in which $\nu = (8kT/\pi m)^{1/2}$ is the mean thermal speed. The constant of proportionality in this expression for D_0 is simply 1/3 for a circular channel but varies as $\ln(\Lambda/a_0)/\sqrt{8}$ for slitlike pores [9–11]. Furthermore, in very small pores measuring only one or two molecular diameters an even slower regime of gas diffusion has been identified by Jepps *et al.* [12].

Ion transport within porous electrodes of capacitors and batteries is also governed by Eq. (1). Here, the flux of ions results mainly from electromigration driven by gradients of the electric potential [13–15]. Thus, the ionic conductivity $(1/\Omega\ \mathrm{cm})$ of the electrolyte is the operative diffusion coefficient, D_0. Further, since the surface charge density is proportional to the electric potential, $\beta_0 \approx 2C/a_0$ where C is the surface capacitance $(\mathrm{F/cm^2})$ and $2/a_0$ is the ratio of pore surface area to pore volume. Thus, the diffusivity, $\alpha_0 = D_0/\beta_0$, tends to increase linearly with pore size [14,15]. In addition, the diffusivity in small pores may increase with increasing pore size due to mitigation of hindrance effects that occur when pore sizes are comparable to the sizes of hydrated ions [18].

Transport along the second and higher levels of the network $(k>0)$ is governed by an equation that resembles Eq. (1) but also includes lateral transport between these channels and the smaller channels of the preceding level.

$$\beta_k \frac{\partial \rho}{\partial t} = D_k \frac{\partial^2 \rho}{\partial x_k^2} + \frac{2}{a_k}\frac{a_{k-1}}{b_{k-1}} D_{k-1} \left.\frac{\partial \rho}{\partial x_{k-1}}\right|_{x_{k-1}=0}. \tag{2}$$

Here, x_k is measured from the channel ends and the factor of $2/a_k$ in the last term is the ratio of surface area to cross-sectional area for a slit. In addition, the lateral diffusion flux in the last term of Eq. (2) is multiplied by the ratio a_{k-1}/b_{k-1} representing the fraction of the channel wall area receiving lateral transport. This continuous approximation of discrete lateral fluxes is well justified because lateral channel spacing, b_{k-1}, is typically much smaller than the channel length, b_{k+1}.

To approximate the discharge/recharge cycle of a storage material we seek solutions of a form appropriate for a sinusoidal variation in the external density having period $1/\omega$, amplitude $\Delta\rho$, and mean density ρ_r.

$$\rho^* = \frac{\rho - \rho_r}{\Delta\rho} = e^{i\omega t} \rho_0^*(x_0^*) \rho_1^*(x_1^*) \rho_2^*(x_2^*) \cdots \rho_N^*(x_N^*). \tag{3}$$

Here, $\rho_0^*(x_0^*)$ describes the variation in ρ^* along the smallest pores; successive $\rho_k^*(x_k^*)$ represent variation along the kth set of transport channels, $x_k^* = 2x_k/b_{k+1}$, and N is the order of the hierarchy. Substitution of this expansion into Eqs. (1) and (2) yields a sequence of ordinary differential equations for $\rho_k^*(x_k^*)$, all having the same basic form,

$$i\hat{\lambda}_k^2 \rho_k^* = \frac{d^2 \rho_k^*}{dx_k^{*2}}. \tag{4}$$

The boundary conditions are also the same for all levels: $\rho_k^* = 1$ at channel entrances where $x_k^* = 0$, and the symmetry condition $d\rho_k^*/dx_k^* = 0$ is applicable at channel midplanes where $x_k^* = 1$. Thus, the same general solution is applicable to all levels of the hierarchy except that the value of the parameter $\hat{\lambda}_k$ differs in a recursive fashion from one level to the next.

$$\rho_k^* = \frac{\cosh \hat{\lambda}_k \sqrt{i}(1 - x_k^*)}{\cosh \hat{\lambda}_k \sqrt{i}}. \tag{5}$$

For the smallest scale pores $(k=0)$, the balance between capacitance and diffusion terms in Eq. (1) leads to a very simple and familiar expression for $\hat{\lambda}_0$.

$$\hat{\lambda}_0 = \lambda_0 = \frac{b_1}{2}\sqrt{\frac{\omega}{\alpha_0}}. \tag{6}$$

However, for the higher order terms $(k>0)$, variations in the diffusion flux are balanced by capacitance and by lateral fluxes from the intersecting channels of the next smaller size. As seen below in Eq. (7), this introduces a new contribution to $\hat{\lambda}_k$ that is proportional to the density gradient in the next smaller channels, $-\hat{\lambda}_{k-1}\sqrt{i}\tanh(\hat{\lambda}_{k-1}\sqrt{i})$, as evaluated from Eq. (5) at the channel intersection, $x_{k-1}^* = 0$.

$$\hat{\lambda}_k = \lambda_k \left[1 + \frac{\phi_{k-1}}{\phi_k}\frac{\beta_{k-1}}{\beta_k}\left(\frac{\hat{\lambda}_{k-1}}{\lambda_{k-1}}\right)^2 \frac{\tanh \hat{\lambda}_{k-1}\sqrt{i}}{\hat{\lambda}_{k-1}\sqrt{i}} \right]^{1/2} \quad \text{for } k>0, \tag{7}$$

where

$$\lambda_k = \frac{b_{k+1}}{2}\sqrt{\frac{\omega}{\alpha_k}} = b_{k+1}^*\left(\frac{\alpha_0}{\alpha_k}\right)^{1/2} = b_{k+1}^*\left(\frac{a_0^*}{a_k^*}\right)^{m/2}. \quad (8)$$

Here, $i=\sqrt{-1}$, $\phi_k=a_k/b_k=a_k^*/b_k^*$, and a_k^* and b_k^* have been normalized by the length scale $(4\alpha_0/\omega)^{1/2}$.

$$a_k^* = \frac{a_k}{2}\sqrt{\frac{\omega}{\alpha_0}} \quad b_k^* = \frac{b_k}{2}\sqrt{\frac{\omega}{\alpha_0}} \quad L^* = \frac{L}{2}\sqrt{\frac{\omega}{\alpha_0}}. \quad (9)$$

The squares of the Fourier moduli, λ_k^2, represent ratios of dynamic response time, b_{k+1}^2/α_k, to cycle time, $1/\omega$, applicable to kth level pores in the absence of lateral losses into pore walls. The $\hat{\lambda}_k^2$'s are normalized response times that account for lateral losses. These expressions entail b_{k+1} because this is the length of the kth level channels; b_{k+1} is also the channel spacing for the $k+1$ level. Note that λ_N is based on the overall size of the medium, $L=b_{N+1}$.

The exponent m appearing in Eq. (8) describes the variation in effective diffusivity, α_k, with channel width, a_k^*. Thus, $m=2$ for a viscous gas flow, $m=1$ for free molecular flow, and $m=0$ for simple diffusion or electromigration. However, since the surface to volume ratio in rectangular slits is $2/a_k$, these exponents increase by unity in cases where channel capacitance is associated mainly with channel surface area, rather than channel volume. Thus, our example calculations will focus on the range $1\leq m\leq 3$. We exclude $m=0$, because in this case wider transport channels provide no benefit [7]. Also, we assume for simplicity that m is constant across all levels of the hierarchy.

The pore structure is optimized using a simplex algorithm to determine values of a_k^* and b_k^* that maximize periodic inflow/outflow from the smallest pores subject to a given system volume. Maximizing periodic flow is equivalent to maximizing the amplitude of the sinusoidal variation in the mean density within the nanopores, $|\Delta\bar{\rho}_0^*|$. This quantity is readily evaluated by spatial integration of the solution given by Eqs. (3) and (5)–(8) over the nanopore volume. Integrating in sequence over each of the x_k^* we obtain

$$|\Delta\bar{\rho}_0^*| = \left|\int\int_0^1 \cdots \int_0^1 \left[\prod_{k=0}^{N}\rho_k^*(x_k^*)\right] dx_0^* dx_1^* \cdots dx_N^*\right| = \left|\prod_{k=0}^{N}\frac{\tanh\hat{\lambda}_k\sqrt{i}}{\hat{\lambda}_k\sqrt{i}}\right|. \quad (10)$$

Here, the vertical bars indicate the amplitudes of the enclosed complex numbers and so represent half of the peak to valley variation in the mean nanopore density. We take credit only for density changes within the nanopores because they provide functionality unavailable in larger pores and they generally account for an overwhelming majority of the pore volume and surface area. Thus, the optimization criterion, Ω, is taken as the product of $|\Delta\bar{\rho}_0^*|$ with the ratio the volume *containing* nanopores to the total system volume.

$$\Omega = |\Delta\bar{\rho}_0^*|\frac{V_{nanopores}}{V_{total}}. \quad (11)$$

The volume ratio appearing here can be calculated by noting that a unit volume containing nanopores is augmented at the first level by an incremental volume, $\phi_1=a_1/b_1$, and that this block of composite volume $(1+\phi_1)$ is augmented at the second level by an incremental volume $\phi_2(1+\phi_1)$, and so on to arrive at the expression

$$\frac{V_{nanopores}}{V_{total}} = \frac{1}{(1+\phi_1)+\phi_2(1+\phi_1)+\phi_3(1+\phi_1)(1+\phi_2)+\cdots}. \quad (12)$$

The nanopore porosity, ϕ_0, and capacitance, β_0, need not be included in the numerator of this expression because they are constants for nanopores of fixed size and so do not influence the optimization. By omitting these constants, we ensure that the object function, Ω, will have a maximum value of unity when two conditions are met: the density within the nanopores closely tracks the applied external density variation (i.e., $|\Delta\bar{\rho}_0^*|\to 1$), and the volume lost to transport channels is negligible (i.e., $\phi_k=a_k^*/b_k^*\to 0$ for all $k>0$). Note that increases in a_1^* or decreases in b_1^* help to increase the term $|\Delta\bar{\rho}_0^*|$ in the numerator of Eq. (11) but these variations also tend to increase the denominator. As a result, Ω has a maximum value for optimal choices of a_1^* and b_1^*.

III. RESULTS

In all of the examples presented here, the geometry of the nanopores is given as $a_0^*=a_0(\omega/4\alpha_0)^{1/2}=10^{-5}$ and $\phi_0=b_0/a_0=0.3$. We begin by exploring cases where all of the capacitance parameters, β_k, are unity, turning later to examples where $\beta_0\gg 1$. Figure 2(a) illustrates the variation in the optimal a_k^* and b_k^* with the normalized size of the storage medium $L^*=L(\omega/4\alpha_0)^{1/2}$ for $m=2$ and $N=4$. The nearly constant slopes indicate power-law variations in channel dimensions with system scale,

$$a_k^* = A_k L^{*p_k} \text{ and } b_k^* = B_k L^{*q_k}. \quad (13)$$

These powers p_k and q_k, remain remarkably constant over many decades.

The spacing b_1^* between first-level transport channels increases very little with L^* indicating that $q_1\ll 1$, particularly when N is large. This is because b_1^* also represents the normalized length of the nanopores having fixed widths a_0^*. Thus, increases in b_1^* must necessarily cause a corresponding increase in the response time $\hat{\lambda}_0^2$ and the density drop $\Delta\rho_0$ within this scale. In contrast, larger scales all benefit from increases in optimal channel widths with increasing L^*, helping to offset the adverse affect of increased channel length.

As seen in Fig. 2(b), the porosities, $\phi_k=a_k/b_k$, associated with individual levels of a hierarchy all increase with normalized system scale, L^*, indicating that optimal channel widths are increasing faster than optimal channel spacing. The ϕ_k have a power-law dependence on L^*, consistent with the linearity of a_k^* and b_k^* on the previous log-log plots. However, it is somewhat surprising to see that all of the ϕ_k in a hierarchy have the same slope. More surprising yet, the ratios of porosity between successive levels, ϕ_{k+1}/ϕ_k, appear to have roughly the same value between all levels of a hierarchy. Moreover, for the special case of $m=2$ all levels have

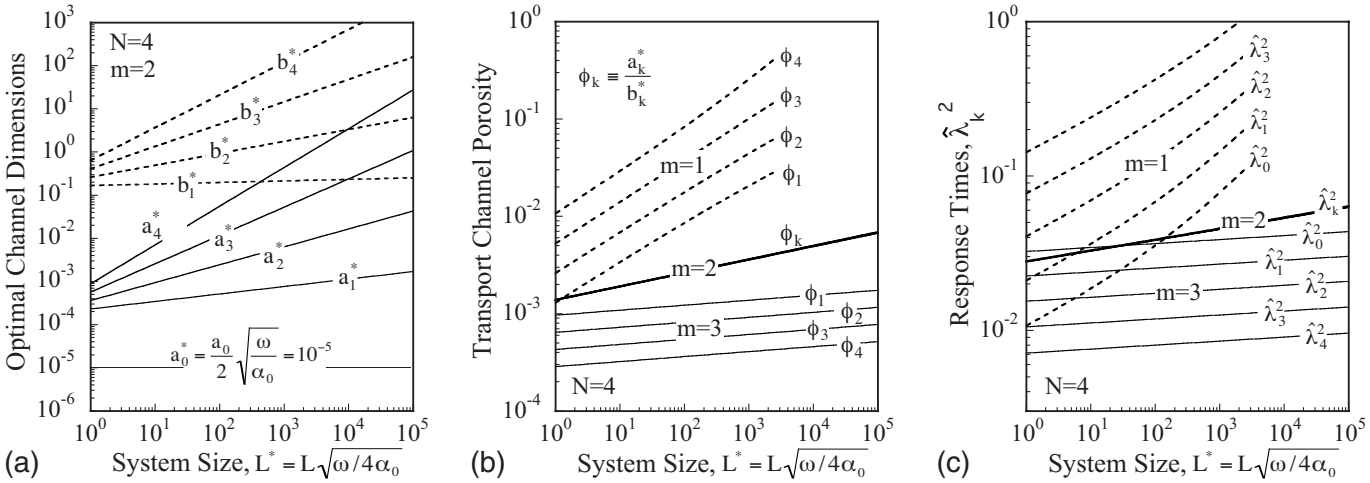

FIG. 2. Channel parameters versus scaled system size: (a) scaled channel widths and spacing, (b) porosity, and (c) scaled response times.

the same porosity. For $m>2$, porosity is greater at higher levels (i.e., large scales), and the converse is true for $m<2$.

The normalized response times, $\hat{\lambda}_k^2$, plotted in Fig. 2(c) share many of the features seen in the preceding plot of porosities. Again, the logarithmic slopes are roughly the same for all levels of a hierarchy and the slopes are nearly constant over the full range of L^*. This power-law behavior suggests that the hyperbolic tangent functions appearing in $\hat{\lambda}_k$ can be well approximated by a one term expansion, an observation we will later exploit. In addition, response times of successive levels, $\hat{\lambda}_{k+1}^2$ and $\hat{\lambda}_k^2$, always have the same ratio, provided that L^* is not too large. As seen earlier for porosities, the $\hat{\lambda}_k$ are identical for all scales of a hierarchy when $m=2$, indicating that all levels have the same response time and that all scales have the same density drop, $\Delta\rho_k$. For other values of m, optimal systems have different response times at different levels, which is perhaps somewhat counterintuitive.

A. Ratios of response times and porosities between levels

The observed ratios of $\hat{\lambda}_k^2$ between hierarchal levels can be explained by an approximate analysis applicable in the limit where L^* is relatively small, such that $\phi_k \ll \phi_0$ and $\tanh \hat{\lambda}_k / \hat{\lambda}_k \approx 1$. In this limit, it follows from Eqs. (7) and (8) that

$$\hat{\lambda}_k \approx \lambda_k \left(\frac{\beta_0\phi_0}{\beta_k\phi_k}\right)^{1/2} = \frac{b_{k+1}^* b_k^{*1/2}}{a_k^{*(1+m)/2}} \left(a_0^{*m}\frac{\phi_0\beta_0}{\beta_k}\right)^{1/2}. \quad (14)$$

The first of these equalities indicates that all levels of the hierarchy respond as though their capacitance is increased by a factor of $\beta_0\phi_0/\beta_k\phi_k$, relative to that of a channel having no lateral losses. This is because each level must carry all of the flow coming to or from the primary capacitance, $\phi_0\beta_0$, that resides within the nanopores. Secondary capacitance within the transport channels ($k>0$) is negligible when $\phi_k \ll \phi_0$. Based on the linearity observed in Fig. 2(c), we make the approximation

$$\frac{\tanh \hat{\lambda}_k\sqrt{i}}{\hat{\lambda}_k\sqrt{i}} \cong 1 - \frac{i}{3}\hat{\lambda}_k^2 \quad (15)$$

so that derivatives of this quantity with respect to $\hat{\lambda}_k$ are proportional to $\hat{\lambda}_k$. Further noting that all of the $\hat{\lambda}_k$ appear symmetrically in $|\Delta\bar{\rho}_0|$, we can write that $\partial|\Delta\bar{\rho}_0|/\partial\hat{\lambda}_k \approx -\Gamma\hat{\lambda}_k$ where a single value of Γ is applicable for all k.

The optimum transport efficiency, Ω, can now be determined by differentiation of Eq. (11) with respect to a_k^* and b_k^* and setting these results to zero.

$$\frac{\partial\Omega}{\partial a_k^*} = \frac{\partial|\Delta\bar{\rho}_0|}{\partial\hat{\lambda}_k}\frac{\partial\hat{\lambda}_k}{\partial a_k^*}\frac{1}{(1+\Sigma\phi_k)} - \frac{1}{(1+\Sigma\phi_k)^2}\frac{\partial\phi_k}{\partial a_k^*} = 0. \quad (16)$$

The derivatives are then expanded using Eqs. (14) and (15) and the relation $\phi_k = a_k^*/b_k^*$ to obtain

$$\frac{\partial\Omega}{\partial a_k^*} = \Gamma\left(\frac{m+1}{2}\frac{\hat{\lambda}_k^2}{a_k^*}\right) - \frac{1}{b_k^*}\frac{1}{(1+\Sigma\phi_k)} = 0. \quad (17)$$

Analogous differentiation with respect to b_k^* yields one additional term because $\hat{\lambda}_k$ and $\hat{\lambda}_{k-1}$ both depend upon b_k^*, as apparent in Eq. (14).

$$\frac{\partial\Omega}{\partial b_k^*} = -\Gamma\left(\frac{\hat{\lambda}_k^2}{2b_k^*} + \frac{\hat{\lambda}_{k-1}^2}{b_k^*}\right) + \frac{\phi_k}{b_k^*}\frac{1}{(1+\Sigma\phi_k)} = 0. \quad (18)$$

The two preceding equations yield a pair of interesting insights. First, elimination of Γ between them provides the following relationship between time constants of successive levels.

$$\frac{\hat{\lambda}_{k+1}^2}{\hat{\lambda}_k^2} = \frac{\hat{\lambda}_k^2}{\hat{\lambda}_{k-1}^2} = \frac{2}{m}. \quad (19)$$

Further, using Eq. (17) by itself one can readily relate ϕ_k to $\hat{\lambda}_k^2$.

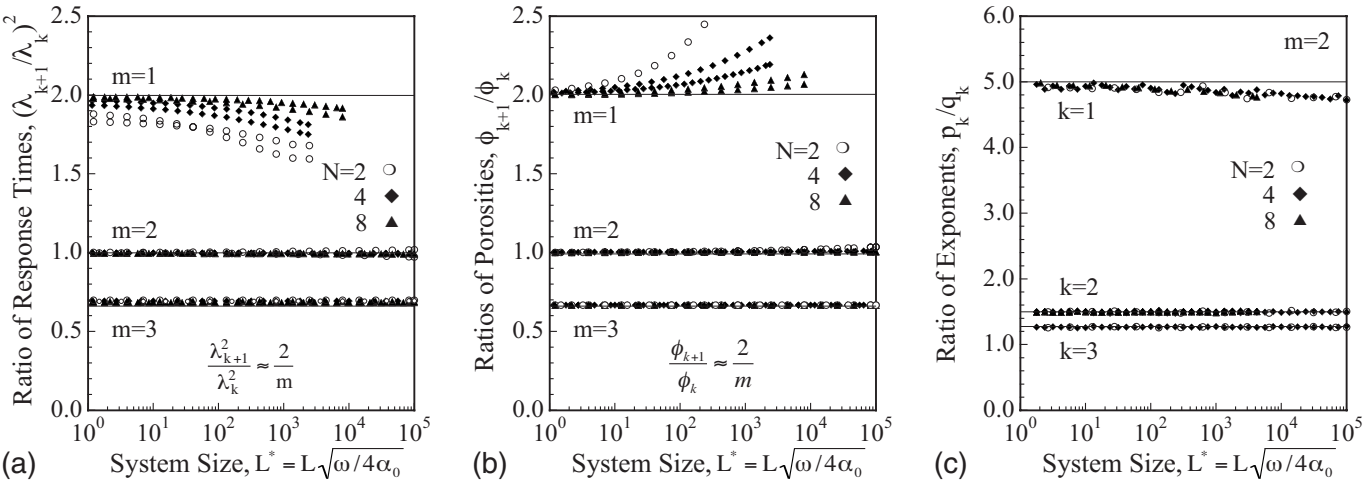

FIG. 3. Ratios of channel parameters versus scaled system size: (a) response times of successive levels, (b) porosities of successive levels, (c) exponents describing variation in channel aperture and spacing with system size.

$$\phi_k = \hat{\lambda}_k^2 \left(\frac{m+1}{2}\right) \Gamma\left(1 + \sum \phi_k\right). \tag{20}$$

Substitution of this result into Eq. (19) yields the ratio of porosities between adjacent levels.

$$\frac{\phi_{k+1}}{\phi_k} = \frac{\hat{\lambda}_{k+1}^2}{\hat{\lambda}_k^2} = \frac{2}{m}. \tag{21}$$

Validity of the preceding relationship between time constants and porosities of successive hierarchical levels is illustrated in Fig. 3(a) and 3(b), respectively. For each value of m, hierarchies having 2, 4, and 8 levels of transport channels were optimized. For each hierarchy, we have plotted $(\hat{\lambda}_2/\hat{\lambda}_1)^2$ and $(\hat{\lambda}_3/\hat{\lambda}_2)^2$ in Fig. 3(a) as a function of normalized system size, L^*. Similarly, Fig. 3(b) displays ϕ_2/ϕ_1 and ϕ_3/ϕ_2, with the latter included only for $N>2$. It is seen that the results for $m=2$ and $m=3$ closely conform to the analytical approximations in Eqs. (19)–(21). The results for $m=1$ appear to be converging toward the expected behavior as L^* becomes smaller but never reach good agreement. This is because the benefits of additional channels are less dramatic for smaller vales of m, making it more difficult to satisfy the approximations made in the asymptotic analysis (e.g., $\tan \hat{\lambda}_k/\hat{\lambda}_k \approx 1$). Consistent with this explanation, the numerical results move toward the analytical approximation as the number of levels in the hierarchy is increased from 2 to 8.

B. Exponents describing variation in a_k^* and b_k^* with L^*

Another remarkable feature of these optimized networks is that the exponents, p_k and q_k, describing the variation in a_k^* and b_k^* with L^* have ratios, p_k/q_k, that are independent of the number, N, of levels in a hierarchy. This is illustrated in Fig. 3(c) for $m=2$, though similar results were obtained for all values of m. In addition, we find that $p_1/q_1 \approx 5$ for all values of m. The fact that a_1^* increases five times faster than b_1^* is expected because $b_1^{*2} = \hat{\lambda}_0^2$ represents the response time of the nanopores and, as such, should increase only weakly with increasing L^*. However, the five-to-one ratio might not be expected to apply so universally to all values of m and N. In [7] it was shown analytically for the special case of $N=1$ that $p_1/q_1=5$ for all values of m. So here, that observation is extended to hierarchies of all order.

Specific values of p_k and q_k that apply for any values of m and N can be deduced from the previously explained ratios of porosities and response times between levels and the observation that $p_1=5q_1$. First, Eq. (14) is used to write the following expression for the ratio $\gamma_k \equiv b_{k+1}^*/b_k^*$:

$$\gamma_k = \frac{b_{k+1}^*}{b_k^*} = \frac{\hat{\lambda}_k a_k^{*m/2} \phi_k \beta_k}{\hat{\lambda}_{k-1} a_{k-1}^{*m/2} \phi_{k-1} \beta_{k-1}} = \left(\frac{2}{m}\right)^{1+m/2} \frac{\beta_k}{\beta_{k-1}} \left(\frac{b_k^*}{b_{k-1}^*}\right)^{m/2}. \tag{22}$$

Here, we replaced the a_k^* with $b_k^* \phi_k$ and then used the relationships $\phi_k/\phi_{k-1}=2/m$ and $\hat{\lambda}_k/\hat{\lambda}_{k-1}=\sqrt{2/m}$ from Eqs. (19) and (21) to replace the ratios of $\hat{\lambda}_k$ and ϕ_k between levels. Equation (22) yields the simple recursion relation $\gamma_{k+1} \propto \gamma_k^{m/2}$. Further, since $L^* = b_1^*(\gamma_1 \gamma_2 \ldots \gamma_{N-1}\gamma_N)$ and since $b_1^* \propto L^{*q_1}$ according to the definition in Eq. (13), it follows that

$$\gamma_1 \propto L^{*(1-q_1)/\Psi} \quad \text{where} \quad \Psi \equiv \sum_{k=1}^{N} (m/2)^{k-1}. \tag{23}$$

Using Eq. (14) for $k=1$ and the identity $\phi_1 = a_1^*/b_1^*$, the proportionality between time constants, $(\hat{\lambda}_0/\hat{\lambda}_1)^2 = 2/m$, can be rewritten as

$$a_1^{*(1+m)/2} \propto \frac{b_2^*}{b_1^{*1/2}} = \frac{b_1^* \gamma_1}{b_1^{*1/2}} = b_1^{*1/2} L^{*(1-q_1)/\Psi}. \tag{24}$$

Now, by introducing the definitions made in Eq. (13), $a_1^* \propto L^{*p_1} = L^{*5q_1}$ and $b_1^* \propto L^{*q_1}$, we can use Eq. (24) to identify the value of q_1 and hence p_1.

$$q_1 = \left[1 + \frac{\Psi}{2}(4+5m)\right]^{-1} \quad \text{and} \quad p_1 = 5q_1. \tag{25}$$

Further, since ϕ_{k+1}/ϕ_k is independent of L, it must be that $p_{k+1} - p_k = q_{k+1} - q_k$. We also have that $L^{*(q_{k+1}-q_k)} \propto \gamma_k$,

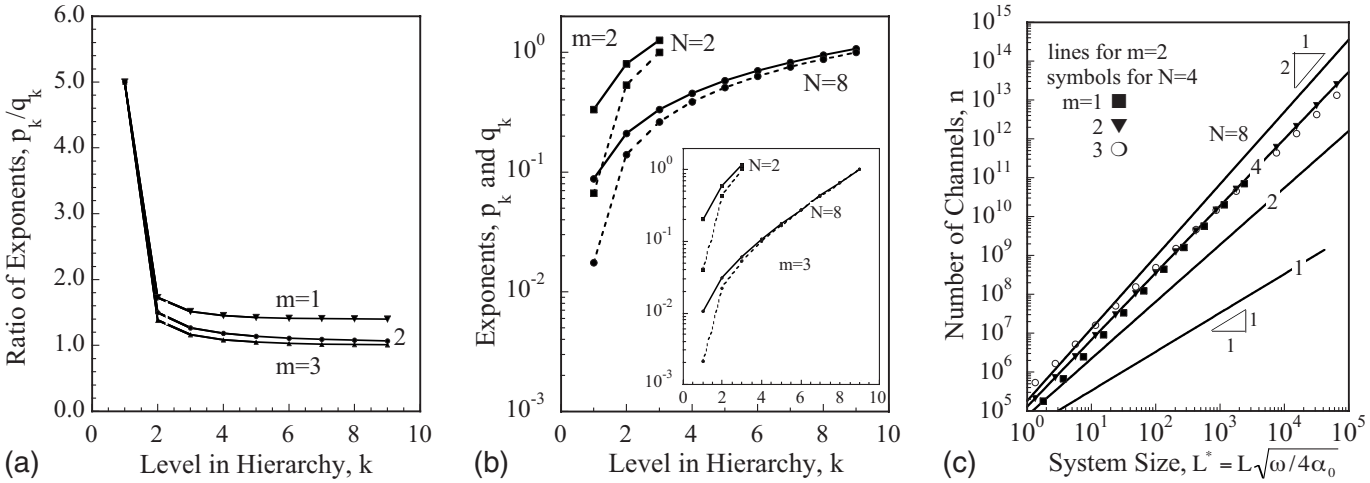

FIG. 4. (a) Analytically determined ratios of exponents, p_k/q_k, versus level in hierarchy, (b) analytical values of exponents versus level in hierarchy, (c) numerically computed number of channels versus system size.

$\gamma_1 \propto L^{*(1-q_1)/\Psi}$, and $\gamma_{k+1} \propto \gamma_k^{m/2}$. These relationships can be combined to yield the following recursion formula for the exponents of higher order terms ($k \geq 1$).

$$q_{k+1} - q_k = p_{k+1} - p_k = \frac{(1-q_1)}{\Psi}\left(\frac{m}{2}\right)^{k-1} = q_1\left(\frac{4+5m}{2}\right)\left(\frac{m}{2}\right)^{k-1}. \tag{26}$$

Validity of the above analytical expressions for the exponents p_k and q_k can be judged, in part at least, from the numerical results shown in Fig. 3(c). The ratio p_1/q_1 is very close to the expected value of five for small values of L^* but drifts gradually downward with increasing L^*. Surprisingly, the drift is about the same for all values of N. In contrast, the numerically calculated ratios of p_2/q_2 and p_3/q_3 are extremely close to the values of 1.5 and 1.267 predicted from Eqs. (25) and (26) for all values of L^* and N.

It is perhaps somewhat curious that the ratios of p_k/q_k are independent of N. This might not be anticipated from a cursory inspection of Eqs. (25) and (26) since Ψ depends upon N. However, as apparent from the last equality in Eq. (26), all of the terms in the summations leading to p_k and q_k are proportional to q_1. Thus, the dependence of p_k and q_k on Ψ arises only through q_1, and this common factor cancels out of the ratios of p_k/q_k.

Ratios of exponents do depend upon m, as illustrated in Fig. 4(a). The values shown there were computed from Eqs. (25) and (26). They apply for all values of N. It is seen that the ratios of p_k/q_k fall abruptly from a value of five for $k=1$ to values around 1.5 for $k=2$. For larger k, there is a gradual approach to an asymptotic value of ~ 1.0 for $m=2$ and $m=3$ indicating that the exponents, p_k and q_k, are the same. For $m=3$, the asymptotic value of p_k/q_k is approximately 1.4 for large values of k.

Values of p_k and q_k are shown in Fig. 4(b). For the range shown they are all less than unity. The exponents both increase with k. The reason for this is relatively clear for q_k since q_1 must be small to maintain a moderate value of the time constant, $\hat{\lambda}_0^2 = b_1^{*2}$, whereas $q_{N+1}=1$ since $b_{N+1}^* = L^*$. In concert with this, the exponents, p_k, of the apertures must apparently be comparable to accommodate the increased flow that accompanies wider spacing. Both exponents decrease when N is larger because a greater number of levels are available to span the gap in length scales between b_1 and L. Similarly, exponents are somewhat smaller when m is larger because increases in channel aperture provide greater benefit when m is larger. This has a greater influence on apertures, and hence p_k rather than q_k.

The total number of channels in a hierarchy is dominated by the number, n, of the smallest scale channels. This quantity is also of interest as it corresponds to the number of nodal points or end points in previously studied vascular or treelike networks. It can be computed as the continued product of the number of channels $n_k = b_{k+1}^*/b_{k-1}^*$ present in each level of a latticelike network. Although n can be estimated very accurately using values of $\gamma_k = b_{k+1}^*/b_k^*$ derived earlier in Eq. (23) and just above, it is perhaps more instructive to pursue the more transparent approximation given below. The rational for this approximation is explained in the text that follows.

$$n = \prod_{k=1}^{N} \frac{b_{k+1}^*}{b_{k-1}^*} = \frac{L_N^*}{b_0^*}\prod_{k=1}^{N-1}\frac{b_{k+1}^*}{b_k^*} \sim \frac{L^*}{b_0^*}\left(\frac{L^*}{b_1^*}\right)^{(N-1)/N} \sim L^{*(2N-1)/N}. \tag{27}$$

To simplify the above product we began by factoring out the ratio of the prescribed values of b_0^* and $b_{N+1}^* = L^*$. The remaining ratios are then written in terms of the $N-1$ values of b_{k+1}^*/b_k^*. Further, from inspection of Fig. 2(a) we see that these ratios are typically distributed about evenly above and below the mean value of $(b_{k+1}^*/b_k^*)_{mean} \sim (L^*/b_1^*)^{1/N}$. Finally, recall that $b_1^* \propto L^{*q_1}$ and that q_k is relatively small to deduce that the number of channels should increase as roughly the $(2N-1)/N$ power of L^*. As seen in Fig. 4(c), this estimate is extremely good for $m=2$; it holds equally well for $m=3$ but

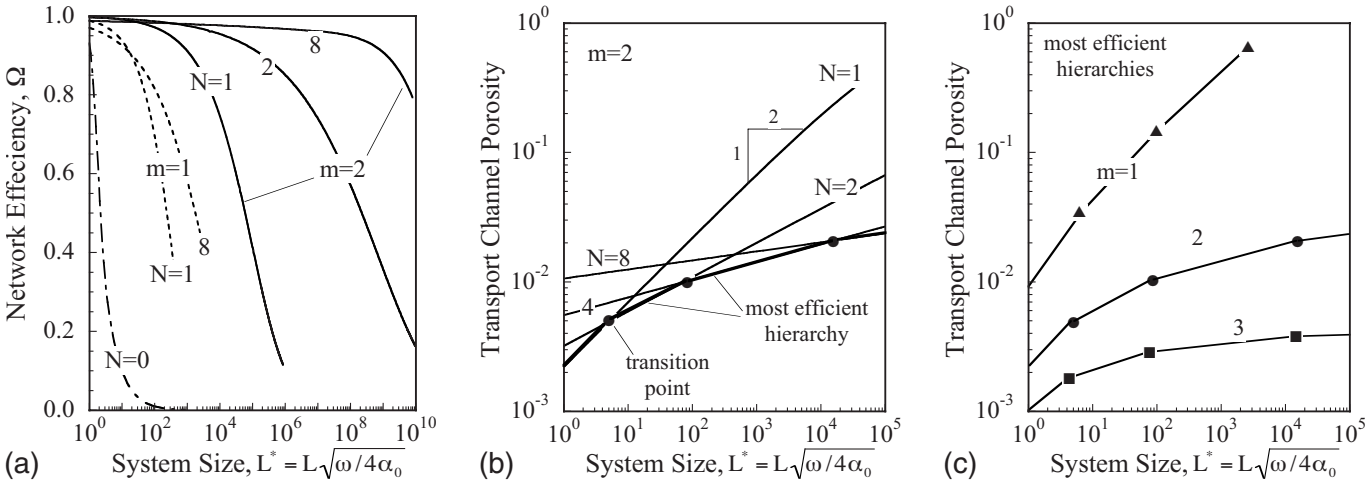

FIG. 5. Network performance parameters versus scaled system size: (a) network efficiency, (b) transport channel porosity, (c) porosity of most efficient hierarchies.

not as well for $m=1$ due to larger variation in b_1^* with L^*; this error is easily corrected by substitution values of q_1 from Eq. (25) into Eq. (27). Note that the slopes on the logarithmic plot in Fig. 4(c) increase from 1 to 2 as N increases from unity to infinity.

C. Transport network efficiency and porosity

Figure 5(a) depicts the variation in optimal network efficiency, Ω, with system size. To achieve Ω near unity, nanopore densities must closely track the imposed external density variation and the volume given to transport channels must be small. Under these conditions all of the gas or electric charge that could possibly be stored within the total system volume is delivered within the time, $1/\omega$, used in scaling L^*. In the absence of transport channels, $\Omega \cong 0.9$ for $L^*=1$, as indicated by the dotted line in Fig. 5(a) for $N=0$. At this point the delivery is still 90% of the maximum possible, but for $L^*>1$ the available delivery or, equivalently, the transport efficiency, Ω, falls off precipitously with increased size or reduced discharge time. With the addition of transport channels (for $m=2$ and $N=2$), $\Omega>0.9$ for $L^*<10^6$, expanding the permissible system size by 10^6.

Additional hierarchical levels often provide added benefit, as illustrated by the results in Fig. 5(a) for $N=8$. But marginal returns diminish with increasing N. Although not included in Fig. 5(a), the benefits of transport channels are even greater for $m=3$. However, for $m=1$, the increase in diffusivity with channel width is weaker. As a result, one or two levels of transport channels can expand permissible system sizes by only $\sim 10^2$ for $m=1$, and additional hierarchical levels are only slightly beneficial, if not detrimental, particularly when L^* is relatively small.

Network efficiency may actually decrease when additional levels of transport channels are added to a hierarchy. This trend, illustrated by the crossing of lines in Fig. 5(a), can be better understood by consideration of the total porosity devoted to transport channels, as this porosity reduces the volume available for nanopore storage. As seen earlier in Fig. 2(b), the increase in transport channel porosity, ϕ_k, with system size is the same for all k. Thus, the total transport channel porosity is proportional to ϕ_1.

$$\phi_{tran} \propto \phi_1 = \frac{a_1}{b_1} \propto L^{*(p_1-q_1)} = L^{*4q_1}. \tag{28}$$

According to Eq. (25), $q_1=1/(1+7N)$ for $m=2$, so the exponents for ϕ are calculated to be $4q_1=0.5$, 0.267, 0.138, and 0.07 for $N=1$, 2, 4, and 8, respectively. As apparent from a careful inspection of Fig. 5(b), these analytical estimates are in excellent agreement with the numerical results indicated by solid lines. It is also seen that when N is larger, the optimal porosity increases more slowly with system size and, in accordance with Fig. 5(a), this translates into greater transport efficiencies for large values of L^*. However, large N may not be beneficial on smaller domains.

Extraneous levels of transport channels may reduce network efficiency because they consume excessive system volume without providing an offsetting reduction in density differences, $\Delta\rho_k^*$. This is apparent in Fig. 5(b) where the transport channel porosity of optimal systems increases with N for small L^* but has the opposite trend for large L^* where additional levels are actually needed. Furthermore, by comparison of Figs. 5(a) and 5(b) it is seen that crossovers in porosity between hierarchical orders correspond well, though not exactly, with crossovers in network efficiency. This observation suggests that the optimal hierarchy having the smallest porosity is generally the most efficient. Thus, for $L^* \leq 5$ the highest efficiency is obtained with $N=1$. Similarly, $N=2$ is preferred in the range $5 \leq L^* \leq 100$, and so on, as indicated by the heavy line connecting the crossover points in Fig. 5(b). The same procedure is used to produce the loci of most efficient networks displayed in Fig. 5(c) for $m=1$, 2, and 3.

D. Analytical solutions for small to moderate L^*

Optimal channel dimensions for all levels of a hierarchy can be computed analytically by combining the results given here with previously derived solutions [7] for a hierarchy

having only one level of transport channels ($N=1$). In that paper, a power series expansion for small L^* yielded the following expressions for a_1^* and b_1^* in terms of $\hat{\phi}_0 = \phi_0\beta_0/\beta_1$, a_0^*, and L^*:

$$a_1^* \approx C_a[a_0^{*m}\hat{\phi}_0 L_{N=1}^{*2}]^{5/(6+5m)} \quad \text{and}$$

$$b_1^* \approx C_b[a_0^{*m}\hat{\phi}_0 L_{N=1}^{*2}]^{1/(6+5m)}. \tag{29}$$

The constants in these expressions are $(C_a, C_b) = (0.78, 0.89)$, (0.99, 1.04), and (1.06, 1.11) for $m=1$, 2, and 3, respectively. Because of the recursive structure of the solutions in Eqs. (5)–(8), each level is dependent only upon those below it. Thus, Eq. (29) still holds for $N>1$ except that the length of the level-one transport channels, denoted $L_{N=1}^*$ in Eq. (29), must be replaced by b_2^* when $N>1$, as apparent in Fig. 1.

The equations given above for a_1^* and b_1^* can be related to L^* for the overall system and to the optimal values of the other a_k^* and b_k^* using Eqs. (14), (19), and (21). To this end we begin by selecting a value of $b_2^*=L_{N=1}^*$ and use this to compute a_1^* and b_1^* from Eq. (29). The ratio of these provides $\phi_1=a_1^*/b_1^*$, and the remaining ϕ_k are given by $\phi_k = (2/m)\phi_{k-1}$ for $k=2,N$ in accordance with Eq. (21). We also have from Eq. (6) that $\hat{\lambda}_0=b_1^*$, which is known, so the remaining $\hat{\lambda}_k$ can be computed recursively as $\hat{\lambda}_k=\hat{\lambda}_{k-1}\sqrt{2/m}$. These values of ϕ_k and $\hat{\lambda}_k$ are then used to sequentially calculate b_{k+1}^* for $k=2,N$ and a_{k+1}^* for $k=1$, $N-1$ based on the following rearrangement of Eq. (14) and the definition of ϕ_k.

$$b_{k+1}^* \approx \hat{\lambda}_k\left(\frac{a_k^*}{a_0^*}\right)^{m/2}\left(\frac{\phi_k\beta_k}{\phi_0\beta_0}\right)^{1/2} \quad \text{and} \quad a_{k+1}^* \approx \phi_{k+1}b_{k+1}^*. \tag{30}$$

Finally, note that recursive application of Eq. (30) has provided the value of $L^*=b_{N+1}^*$ corresponding to our initial choice of b_2^*. This process can be very easily repeated for a broad range of b_2^* to map out values of the optimal parameters as an implicit function of L^* for any choice of N.

In Fig. 6 the above analytical approximations (solid lines) are seen to compare very favorably with numerical calculations (symbols) of optimum apertures for $N=2$. The upper two lines indicate a_1^* and a_2^* for $m=1$ while the lower two lines are for $m=3$. As expected for an asymptotic expansion, the accuracy of the approximation begins to deteriorate with increasing L^*, as apparent in the uppermost line on Fig. 6. The spacing of the numerical calculations for $m=1$ was increased (closer symbols) when the optimal apertures exceeded the corresponding spacing, indicating a transport efficiency of less 50%, ($\Omega<0.5$). Typically, the analytical results are reasonably accurate up to this point, and there is generally little need to go far beyond this into regions of lower efficiency. Agreement between analytical and numerical results is equally good for calculations of the optimal spacing, b_k^*, and for alternative choices of m and N and the other parameters. It is interesting to note that the slopes of all the solid lines in Fig. 6 are correctly captured by the above calculational procedure, even though there was no explicit use of the exponents derived earlier.

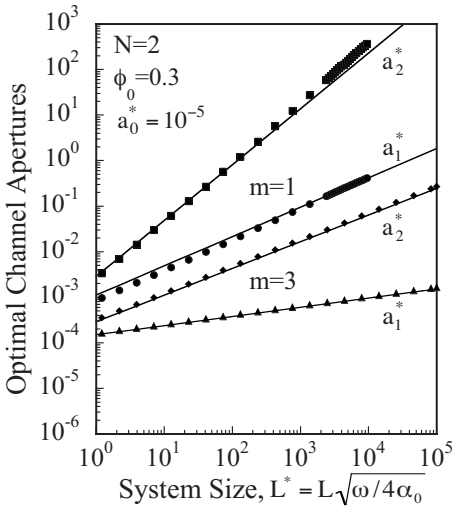

FIG. 6. Comparison of analytical approximations (solid lines) with numerical calculation (symbols) of optimal apertures for $N=2$ and $m=1$ and 3.

E. Differing capacitance of nanopores and transport channels

In porous materials having multiple scales of porosity the mechanism of energy storage may differ substantially between the smallest nanopores and the larger transport channels. For example, the close confinement of nanopores causes condensation of gases at pressures far smaller than nominal condensation pressures operative in pores that are several times wider. Similarly, one or two molecular layers of adsorbed gases or charged ions may account for most of the capacitance in very small pores, while the same layers would represent a negligible portion of the overall capacitance in pores two or three orders larger. To account for these alternative storage mechanism, the transport equations, Eqs. (1) and (2), include capacitance terms, β_k, that may differ among levels of the hierarchy.

To explore the influence of differing capacitance mechanisms, results are presented in Fig. 7 for several values of the ratio of nanopore capacitance to that of the transport channels, $\beta^*=\beta_0/\beta_1$. As in all preceding calculations, $\beta_k=1$ for $k>0$. For the example illustrated in Fig. 7(a), the optimal channel spacing, b_k^*, increases with β^*, but these variations are less than twofold for a thousandfold increase in β^*. Optimal apertures, a_1^*, increase as roughly the cube root of β^*, while a_2^* has a slightly weaker dependence. These increases in aperture are necessary because the volumetric flow carried by the transport channels is proportional to β^*.

Fourier moduli, $\hat{\lambda}_k$, representing square roots of response times of the first two hierarchical levels are presented in Fig. 7(b) for $m=1$, 2, and 3. Except for a moderate increase in the values of $\hat{\lambda}_k$, nothing is substantially altered by a hundredfold increase in β^*. The slopes and the spacing of the lines appear to be essentially independent of β^*, as one would expect from the analysis presented in Eqs. (14)–(21). As before, all of the $\hat{\lambda}_k$ are identical when $m=2$. Qualitatively, little is changed so long as L^* remains small enough that the transport channel porosity is less than about 10–20 % such

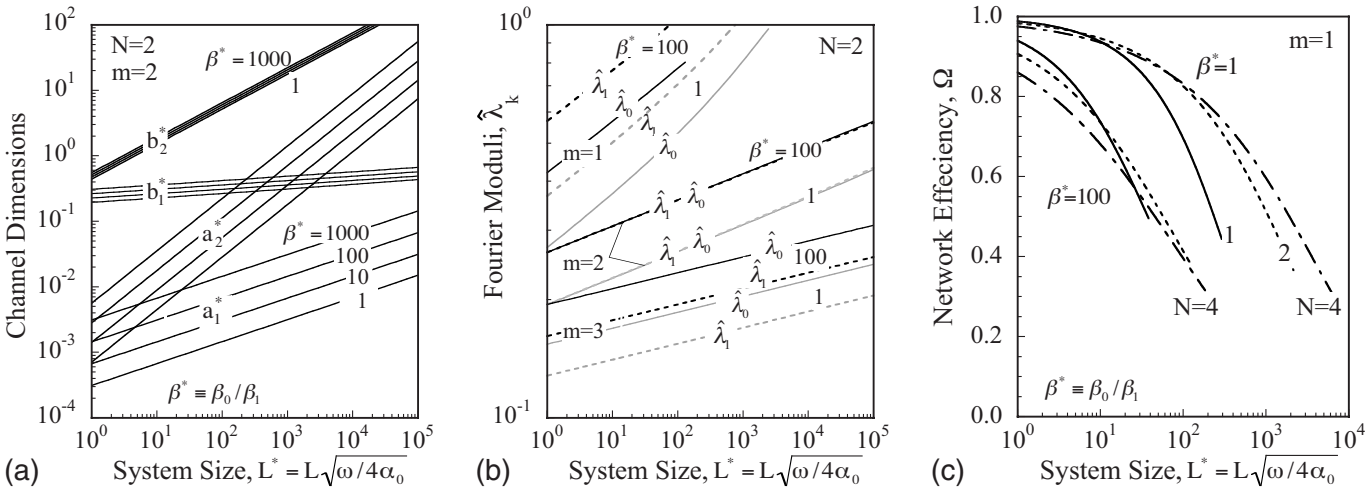

FIG. 7. Influence of capacitance ratio, β^*, on (a) scaled channel widths and spacing, (b) Fourier Moduli, and (c) network efficiency.

that network efficiency is greater than about 75% and, under these conditions, the logarithmic plots in Figs. 7(a) and 7(b) remain relatively linear.

The strongest influence of large nanopore capacitance, $\beta^* \gg 1$, is that network efficiency, Ω begins to fall off at smaller values of the normalized system scale, L^*, as apparent in Fig. 7(c). Here, it appears that a hundredfold increase in β^* causes a reduction in permissible system sizes by a factor of 10 to one hundred for $N=1-4$. These results for $m=1$ are more severe than for larger values of m where increases in aperture provide more benefit.

Aside from the considered cases where capacitance ratios are prescribed, these ratios are sometimes a function of the pore size such that $\beta_k/\beta_o=(a_k/a_0)^\theta$. For example, when surface capacitance is dominant over multiple scales of a hierarchy, β_k is inversely proportional to channel aperture so that $\theta=-1$. For nonzero θ, the approximation made in Eq. (14) we can rewritten as

$$\hat{\lambda}_k^2 \approx \lambda_k^2\left(\frac{\beta_0\phi_0}{\beta_k\phi_k}\right) \propto \frac{b_{k+1}^{*2}}{4}\left(\frac{a_0}{a_k}\right)^m \frac{\phi_0}{\phi_k}\frac{\beta_0}{\beta_k} = \frac{b_{k+1}^{*2}}{4}\frac{\phi_0}{\phi_k}\left(\frac{a_0}{a_k}\right)^{m+\theta}. \tag{31}$$

Thus, the power $m+\theta$ plays the role of m and the equations are essentially the same as before, provided that $m+\theta>0$. In the special case where $m+\theta=0$, this parameter is no longer influential, but there still exist optimum values of the porosities, $\phi_k=a_k/b_k$, as discussed in [7] for $N=1$. In the unlikely circumstance that $m+\theta<0$, hierarchical networks would provide no benefit because increasing channel sizes would impede transport.

IV. SUMMARY AND CONCLUDING REMARKS

Analytical solutions describing periodic response of hierarchical transport networks have been used to identify channel apertures and spacing yielding maximum extraction of gas or electric charge stored within a permeable medium. These optimal channel dimensions depend upon the size of the system relative to the desired extraction duration. As a consequence, no multiscale storage material can be ideally suited for all applications. If slow extraction is acceptable, optimal transport channels will be narrower and sparser, leaving more of the system volume for high-density storage within nanopores. Conversely, systems optimized for rapid extraction will have wider more closely spaced transport channels, less nanopore volume, and less storage capacity.

Optimal channel dimensions were found to increase in a power-law fashion with scaled system size. Analytical expressions for the correspond growth-rate exponents were found to depend only upon the exponent m relating the transport diffusivity to channel aperture; surprisingly, they do not depend on the number of levels, N, in the hierarchy. Analytical expressions for the optimal channel dimensions were derived and were found to be reasonably accurate within the range of greatest interest where transport efficiency is greater than 50%.

Despite these variations in optimal channel dimensions with scaled system size, key structural parameters do not vary with scale, with level within a hierarchy, or with the number of hierarchical levels. In particular, ratios of transport channel porosity between levels depend only upon m.

$$\frac{\phi_{k+1}}{\phi_k} \equiv \frac{a_{k+1}/b_{k+1}}{a_k/b_k} = \frac{a_{k+1}/a_k}{b_{k+1}/b_k} = \frac{2}{m}. \tag{32}$$

Thus, an optimal network will have a self-similar fractal-like structure only for a quadratic dependence of effective diffusivity on channel width ($m=2$). For other values of m optimal channel widths and spacing increase by different factors between successive levels. Curiously, ratios of normalized response times between hierarchical levels are also found to depend upon this same factor.

$$\frac{\hat{\lambda}_{k+1}^2}{\hat{\lambda}_k^2} \sim \frac{(b_{k+2}^2/a_{k+1}^m)(\phi_0/\phi_{k+1})}{(b_k^2/a_k^m)(\phi_0/\phi_k)} = \frac{2}{m}. \tag{33}$$

As a result, it is only for $m=2$ that all scales have the same response time.

Physically, optimal performance requires that all network levels have comparable response times, $\hat{\lambda}_k^2$, or equivalently, a matching of dynamic impedance or a parity of density differences $\Delta\rho_k$ across scales. If any level responds much slower than the others, channel widths in that level can be increased at the expense of the other levels to obtain better balance. For $m=2$, self-similar networks happen to provide equality of response times. However, for $m>2$ self-similar scaling would lead to relatively slow response at the smaller scales, requiring allocation of more porosity to the smaller scales, as apparent in Fig. 2(b). The opposite trends apply for $m<2$. Remarkably, the optimal balance always involves adjustments in porosity by a factor of $2/m$ between scales and leaves a disparity of $2/m$ in response times of adjacent scales.

ACKNOWLEDGMENTS

The authors appreciate support from the Engineering Sciences Research Foundation at Sandia National Laboratories, a multiprogram laboratory operated by Sandia Corporation, a Lockheed Martin Co., for the U.S. DOE National Nuclear Security Administration under Contract No. DE-AC04-94AL85000.

[1] G. B. West, J. H. Brown, and B. J. Enquist, Science **276**, 122 (1997).
[2] J. R. Banavar, A. Maritan, and A. Rinaldo, Nature (London) **399**, 130 (1999).
[3] A. Bejan and S. Lorente, J. Appl. Phys. **100**, 041301 (2006).
[4] F. Okkels and H. Bruus, Phys. Rev. E **75**, 016301 (2007).
[5] M. Durand, Phys. Rev. Lett. **98**, 088701 (2007).
[6] S. Bohn and M. O. Magnasco, Phys. Rev. Lett. **98**, 088702 (2007).
[7] R. H. Nilson and S. K. Griffiths, Phys. Rev. E **79**, 036304 (2009).
[8] A. S. Arico, P. Bruce, B. Scrosati, J.-M. Tarascon, and W. Van Schalkwijk, Nature Mater. **4**, 366 (2005).
[9] G. Karniadakis, A. Beskok, and N. Aluru, *Microflows and Nanoflows: Fundamentals and Simulation* (Springer, New York, 2005).
[10] C. Cercignani and A. Daneri, J. Appl. Phys. **34**, 3509 (1963).
[11] F. Sharipov, J. Micromech. Microeng. **9**, 394 (1999).
[12] O. G. Jepps, S. K. Bhatia, and D. Searles, Phys. Rev. Lett. **91**, 126102 (2003).
[13] M. W. Verbrugge and P. Liu, J. Electrochem. Soc. **152**, D79 (2005).
[14] R. deLevie, Electrochim. Acta **8**, 751 (1963).
[15] H. Sakaguchi and R. Baba, Phys. Rev. E **76**, 011501 (2007).
[16] *Adsorption and Transport at the Nanoscale*, edited by N. Quirke (CRC Press, Taylor and Francis, Boca Raton, FL, 2006).
[17] G. Q. Lu and X. S. Zhao, *Nanoporous Materials: Science and Engineering* (Imperial College Press, London, 2004).
[18] P. Dechadilok and W. M. Deen, Ind. Eng. Chem. Res. **45**, 6953 (2006).